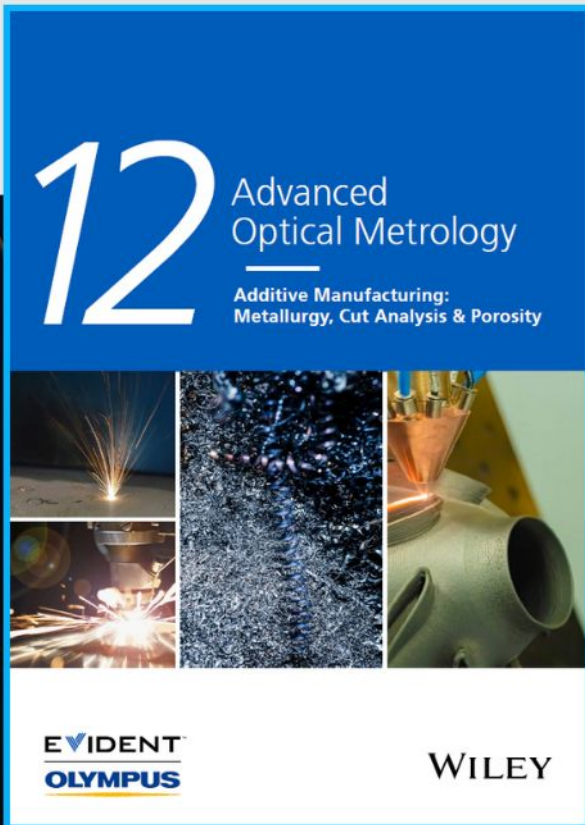




# Additive Manufacturing: Metallurgy, Cut Analysis & Porosity



The latest eBook from  
**Advanced Optical Metrology.**  
Download for free.

In industry, sector after sector is moving away from conventional production methods to additive manufacturing, a technology that has been recommended for substantial research investment.

Download the latest eBook to read about the applications, trends, opportunities, and challenges around this process, and how it has been adapted to different industrial sectors.

**EVIDENT**  
**OLYMPUS**

**WILEY**

# Site-Specific Axial Oxygen Coordinated FeN<sub>4</sub> Active Sites for Highly Selective Electroreduction of Carbon Dioxide

Ting Zhang,\* Xu Han, Hong Liu, Martí Biset-Peiró, Jian Li,\* Xuan Zhang, Pengyi Tang, Bo Yang, Lirong Zheng,\* Joan Ramon Morante, and Jordi Arbiol\*

Regulating the coordination environment via heteroatoms to break the symmetrical electronic structure of M-N<sub>4</sub> active sites provides a promising route to engineer metal-nitrogen-carbon catalysts for electrochemical CO<sub>2</sub> reduction reaction. However, it remains challenging to realize a site-specific introduction of heteroatoms at atomic level due to their energetically unstable nature. Here, this paper reports a facile route via using an oxygen- and nitrogen-rich metal-organic framework (MOF) (IRMOF-3) as the precursor to construct the Fe-O and Fe-N chelation, simultaneously, resulting in an atomically dispersed axial O-coordinated FeN<sub>4</sub> active site. Compared to the FeN<sub>4</sub> active sites without O coordination, the formed FeN<sub>4</sub>-O sites exhibit much better catalytic performance toward CO, reaching a maximum FE<sub>CO</sub> of 95% at -0.50 V versus reversible hydrogen electrode. To the best of the authors' knowledge, such performance exceeds that of the existing Fe-N-C-based catalysts derived from sole N-rich MOFs. Density functional theory calculations indicate that the axial O-coordination regulates the binding energy of intermediates in the reaction pathways, resulting in a smoother desorption of CO and increased energy for the competitive hydrogen production.

## 1. Introduction


Electrochemical CO<sub>2</sub> reduction reaction (CO<sub>2</sub> RR) into CO, which represents a crucial raw product in Fischer-Tropsch process for the production of value-added chemical feedstocks, is considered as a promising route for energy conversion and carbon recycling.<sup>[1-6]</sup> However, the inertness of CO<sub>2</sub> molecule and the competitive hydrogen evolution reaction (HER) greatly limit the conversion efficiency toward the practical implementation.<sup>[7-9]</sup> Atomically dispersed transition metals embedded in nitrogen-doped carbon matrices (M-N-C) have recently appeared at the forefront of CO<sub>2</sub> RR toward CO because of their feasible preparation, optimized atomic utilization and chemical stability.<sup>[10-14]</sup> Based on previous studies, the four-coordinated M-N<sub>4</sub> moieties are considered as the main active centers in common M-N-C.<sup>[15,16]</sup>

T. Zhang, X. Han, J. Arbiol  
Catalan Institute of Nanoscience and Nanotechnology (ICN2)  
CSIC and BIST Campus UAB  
Bellaterra, 08193 Barcelona, Catalonia, Spain  
E-mail: ting.zhang@icn2.cat; arbiol@icrea.cat

T. Zhang, M. Biset-Peiró, J. R. Morante  
Energy Storage  
Harvesting and Catalysis Group  
Catalonia Institute for Energy Research (IREC)  
Sant Adrià de Besòs, 08930 Barcelona, Catalonia, Spain

H. Liu, B. Yang  
School of Physical Science and Technology  
ShanghaiTech University  
393 Middle Huaxia Road, Shanghai 201210, P. R. China

J. Li  
Laboratory of Renewable Energy Science and Engineering  
Institute of Mechanical Engineering  
EPFL, Station 9, 1015 Lausanne, Switzerland  
E-mail: jian.li@epfl.ch

 The ORCID identification number(s) for the author(s) of this article can be found under <https://doi.org/10.1002/adfm.202111446>.

© 2022 The Authors. Advanced Functional Materials published by Wiley-VCH GmbH. This is an open access article under the terms of the Creative Commons Attribution-NonCommercial License, which permits use, distribution and reproduction in any medium, provided the original work is properly cited and is not used for commercial purposes.

DOI: 10.1002/adfm.202111446

X. Zhang  
Department of Materials Engineering  
KU Leuven  
Kasteelpark Arenberg 44, B-3001 Leuven, Belgium

P. Y. Tang  
State Key Laboratory of Information Functional Materials and 2020 X-Lab  
Shanghai Institute of Microsystem and Information  
Technology, Chinese Academy of Sciences  
Shanghai 200050, P. R. China

L. R. Zheng  
Beijing Synchrotron Radiation Facility  
Institute of High Energy Physics  
Chinese Academy of Sciences  
Beijing 100049, P. R. China  
E-mail: zhenglr@ihep.ac.cn

J. R. Morante  
Department of Physics  
Universitat de Barcelona  
Barcelona, 08028 Catalonia, Spain

J. Arbiol  
ICREA  
Pg. Lluís Companys 23  
Barcelona, 08010 Catalonia, Spain

However, the high structure/electron symmetry of the M-N<sub>4</sub> moiety, which results from the symmetrical planar structure, makes it chemically inert to a certain extent.<sup>[17]</sup> Recently, the performance of M-N<sub>4</sub> moiety for CO<sub>2</sub> RR has been significantly improved through the introduction of an additional axial N ligand.<sup>[18–20]</sup> Such coordination can break the symmetrical electronic structure of M-N<sub>4</sub> and subsequently affect the binding energies for CO<sub>2</sub> RR intermediates (e.g., \*COOH and \*CO), which confirmed the key role of axial coordination.<sup>[21]</sup> Inspired by this, it is anticipated that the catalytic activity of M-N<sub>4</sub> can be further boosted by introducing high-electronegativity atoms, such as O, in the axial direction. The high electronegativity of oxygen will not only break the electron symmetry, but also improve the strength of the electronic metal-support interaction (EMSI) in M-N<sub>4</sub> sites.<sup>[21–23]</sup> Unfortunately, the coordination configuration of oxygen atoms is difficult to be controlled accurately via traditional calcination methods. The type of oxygen will change and eventually disappear when the calcination temperature is above 500 °C, which as a consequence hinders the successful coordination of O atoms with the metal site.<sup>[22]</sup> Therefore, developing an effective method to realize the control on O atoms coordination, especially along the axial direction is highly desirable.

Built by metal ions and organic ligands, metal–organic frameworks (MOFs) are recognized as one of the most promising templates for the targeted creation of MN<sub>4</sub> sites.<sup>[24–28]</sup> More importantly, the coordination of heteroatoms (e.g., O, S, P, etc.) can be easily achieved after pyrolysis via the rational design of organic linkers with functional groups.<sup>[25]</sup> Herein,

we propose a facile strategy, which uses an O- and N-rich isorecticular metal–organic framework-3 (IRMOF-3) for constructing an axial O coordination to the FeN<sub>4</sub> active sites. In comparison with FeN<sub>4</sub> structure, the as-prepared axial O-coordinated FeN<sub>4</sub> (denoted as O-Fe-N-C) active sites showed an excellent CO<sub>2</sub> RR activity in 0.5 M NaHCO<sub>3</sub> solution, including a high Faradaic efficiency of CO (95%) at –0.50 V versus reversible hydrogen electrode (RHE), and a robust stability for 30 h. Such performance is superior to those of the previously reported Fe-N-C-based materials and comparable to the reported state-of-the-art single atom catalysts (SACs) even at a lower overpotential. Density functional theory (DFT) calculations revealed that the formed O-Fe-N-C not only facilitates CO desorption, but also limits the undesired HER. This work opens a new way of utilizing heteroatom-rich MOFs as an enabler to the rational design and development of high-efficient catalysts.

## 2. Results and Discussions

### 2.1. Characterization of O-Fe-N-C

The synthesis steps for O-Fe-N-C were schematically displayed in **Figure 1A**. In brief, the Fe-IRMOF-3 was firstly prepared by adding FeCl<sub>3</sub> into IRMOF-3. Afterward, the O-Fe-N-C was obtained through pyrolysis of the Fe-IRMOF-3 under argon atmosphere. A reference Fe-N-C sample without O coordination was also synthesized through pyrolysis of an Fe-based zeolitic

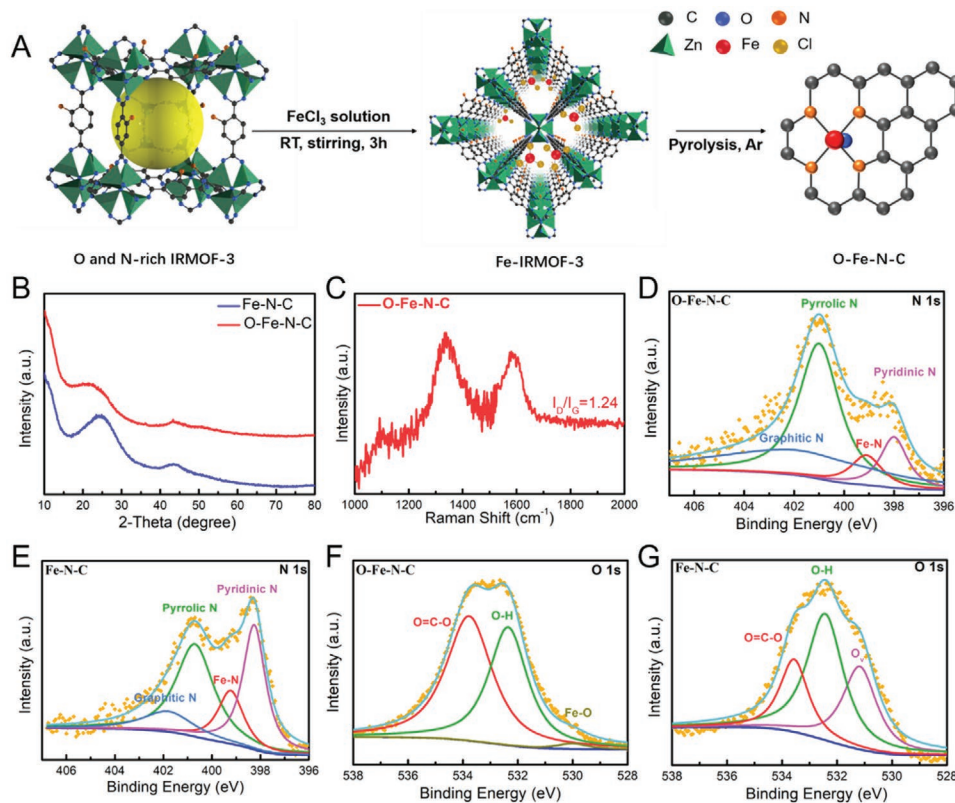


**Figure 1.** A) Schematic illustration of synthesis of O-Fe-N-C. B) XRD patterns of O-Fe-N-C and Fe-N-C samples. C) Raman spectra of O-Fe-N-C. D,E) High-resolution XPS N 1s spectrum, as well as F,G) O 1s spectrum of O-Fe-N-C and Fe-N-C samples.

imidazolate framework (Fe-ZIF-8) precursor prepared by adding  $\text{FeCl}_3$  into N-rich ZIF-8. Two main peaks at around  $25^\circ$  and  $43^\circ$  (Figure 1B), which belong to the (002) and (100) planes of graphitic carbon, were observed in O-Fe-N-C samples, indicating the successful conversion of MOFs into carbon-based materials without the metal, metal oxide, or metal carbide impurity structures.<sup>[29,30]</sup> Similar result was also observed on the X-ray diffraction (XRD) patterns of Fe-N-C sample. The Raman spectra of O-Fe-N-C samples, featuring peaks at around  $1365\text{ cm}^{-1}$  (D band) and  $1590\text{ cm}^{-1}$  (G band), further confirmed the structure of graphitic carbon (Figure 1C).<sup>[31,32]</sup> X-ray photoelectron spectroscopy (XPS) analysis was performed to investigate the chemical composition and elemental states of different samples. The high-resolution N 1s spectra obtained on both the O-Fe-N-C and Fe-N-C samples demonstrate the presence of pyridinic (398.6 eV), pyrrolic (401 eV), graphitic (402 eV), and Fe-N<sub>x</sub> (399.4 eV) species (Figure 1D,E).<sup>[23,30]</sup> In contrast to Fe-N-C (Figure 1G), an additional peak at 530 eV, corresponding to the Fe–O bond, was observed on sample O-Fe-N-C (Figures 1F), which indicated that the Fe-O chelation in O-Fe-N-C sample was retained after calcination.<sup>[22,23,33]</sup>

The O-Fe-N-C sample was further characterized by aberration corrected (AC) high-angle annular dark-field scanning transmission electron microscopy (HAADF STEM). Multiple areas of the O-Fe-N-C sample were examined and only few Fe nanoparticles

could be observed (Figure S2, Supporting Information). Furthermore, AC HAADF STEM was used for directly detecting the single Fe atoms distribution thanks to the different Z contrast among Fe, N, O, and C elements. The representative HAADF STEM images showed isolated starry spots densely planted in the graphitic structure, which confirmed that Fe was atomically dispersed in the O-Fe-N-C sample (Figure 2A,B and Figure S3, Supporting Information). Notice that the graphitic structure showed the typical (001) basal planes, which bend forming layered structures. In addition, the Fe atoms were mainly placed along these basal planes in a perfect single metal atom distribution (see in Figure 2B the red arrows pointing to the C-graphitic (001) planes, while the orange circles highlight the presence of single Fe atoms). Energy dispersive X-rays spectroscopy (EDS) analyses revealed that Fe, N, O, and C were homogeneously dispersed on the O-Fe-N-C sample (Figure 2C and middle panel in Figure 2, as well as Figure S4, Supporting Information). As a comparison, the morphology, elemental distribution and structural HAADF STEM characterization of Fe-N-C and N-C samples is shown in Figures S5 and S6 (Supporting Information).

The detailed local chemical environment and electronic states of the Fe atoms in the catalysts was further disclosed via X-ray absorption spectroscopy analyses. Fe K-edge X-ray absorption near edge structure (XANES) spectra of O-Fe-N-C sample shifts toward higher binding energy compared to that of a

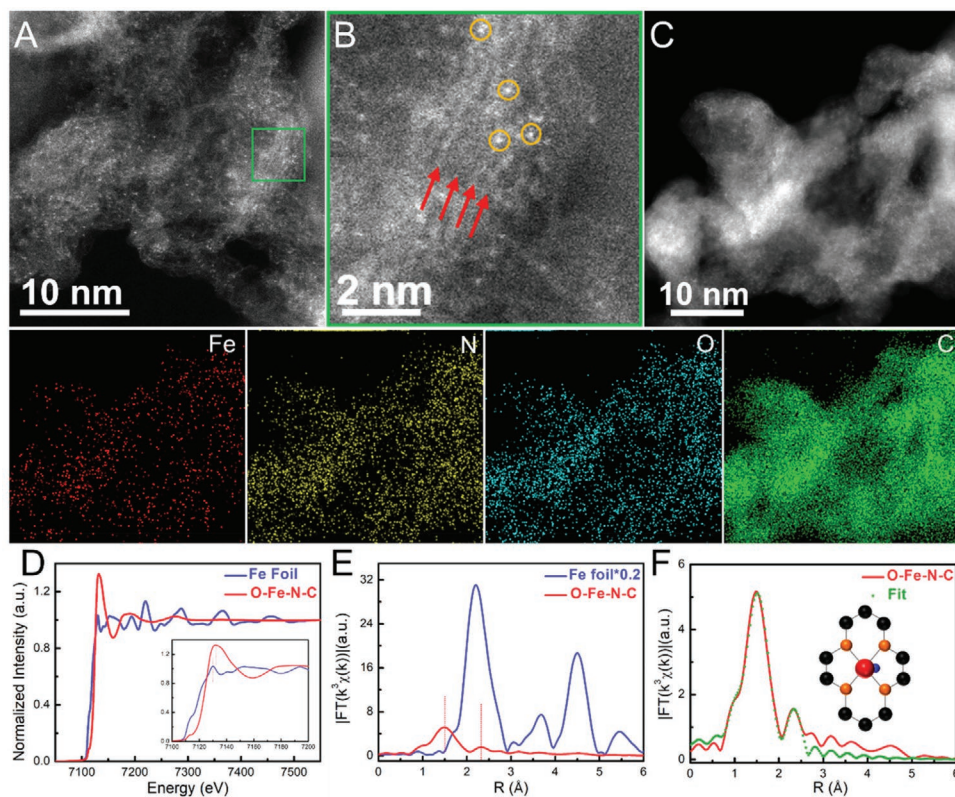


**Figure 2.** A) Atomic resolution aberration-corrected HAADF STEM image obtained on a representative region of O-Fe-N-C catalyst. B) Magnified detail from (A) where the graphitic (001) planes can be observed (red arrows). Notice that dispersed Fe atoms (some of the highlighted with orange circles) are placed along the graphitic structures. C) HAADF STEM image and (middle panel) representative EDS chemical composition maps in a selected region of the O-Fe-N-C sample. D) Fe K-edge XANES spectra, E) Fourier transformation of the EXAFS spectra at R space. F) Corresponding EXAFS fitting curves for the O-Fe-N-C sample (Fe, O, N, and C atoms are represented in red, blue, orange, and black, respectively).

standard Fe foil (Figure 2D), suggesting a positive charge state of Fe atoms in the O-Fe-N-C catalyst.<sup>[34,35]</sup> Furthermore, the intrinsic structure of the reactive sites was corroborated by the Fourier transformed (FT)  $k^3$ -weighted  $\chi(k)$ -function of the Fe K-edge extended X-ray absorption fine structure (EXAFS) in R space (Figure 2E). The dominant peak centered at around 1.5 Å for O-Fe-N-C sample was attributed to the light backscattering induced by light atoms (N, O, or C) situated in the first coordination shell of the absorbing metal. The slight presence of a peak at  $\approx 2.27$  Å, corresponding to the Fe–Fe bond, confirmed a co-existence of the atomically isolated Fe dispersion with a modicum presence of Fe nanoparticles, in accordance with the HAADF STEM results (Figure S2, Supporting Information).<sup>[14,31]</sup> The Fe K-edge EXAFS spectra were then fitted with the model structures depicted in the insets of Figure 2F. The structural parameters obtained from the fittings are shown in Table S1 (Supporting Information), including the coordination number (CN) and different bond distances. The optimized fitting results for O-Fe-N-C sample showed a CN-value of 5.1 and a mean bond length of 2.02 Å. Therefore, there are five coordination atoms around the Fe atoms in O-Fe-N-C sample, which differs from the previously reported M-N<sub>4</sub> sites derived from ZIF-8.<sup>[8,36–40]</sup> Experimentally and theoretically, metal-nitrogen bonds are more likely than metal-carbon or metal-oxygen ones to form in-plane FeN<sub>4</sub> sites in the first coordination sphere.<sup>[17,41]</sup> The higher average CN-value of 5 for Fe-N<sub>4</sub> catalysts strongly suggests that one axial O atom is coordinated in the axial direction of the FeN<sub>4</sub> moieties, resulting in coordinatively saturated iron cations, in line with the high oxophilicity of Fe.<sup>[33,41,42]</sup> In this way, all the results obtained on the O-Fe-N-C sample revealed the presence of four in-plane nitrogen atoms and one oxygen atom as an axial coordination.

## 2.2. CO<sub>2</sub> RR in H-Type Cell

The catalytic performance of the different samples was studied systematically in 0.5 M NaHCO<sub>3</sub>. First, the cyclic voltammetry (CV) curves were carried out to roughly evaluate the electrocatalytic CO<sub>2</sub> RR performance. As shown in Figure S7 (Supporting Information), upon saturating the solution with CO<sub>2</sub>, the increased reduction current on all samples suggested an efficient catalytic performance toward CO<sub>2</sub> RR. Compared to N-C without Fe atoms, the total current densities of O-Fe-N-C and Fe-N-C increased significantly at a wide range of applied potentials, indicating the crucial role of the Fe metal center in CO<sub>2</sub> RR (Figure 3A).<sup>[43]</sup> As expected, the best faradaic efficiency (FE) toward CO in a potential range from –0.40 to –0.70 V versus RHE was obtained for O-Fe-N-C, reaching the maximum FE (CO) of 95% at –0.50 V versus RHE (Figure 3B), which is superior to those of previously reported Fe-N-C-based catalysts and comparable to the state-of-the-art SACs even at lower overpotential (Table S4, Supporting Information). The decreasing trend of FE (CO) for all samples as the potential shifted to more negative values mainly stems from the dominance of the H<sub>2</sub> evolution over the CO<sub>2</sub> RR (Figure 3C). The sums of FE for CO and H<sub>2</sub> are  $\approx 100\%$  for all samples, which indicates that no other products were produced. The potential-dependent CO/H<sub>2</sub> partial current densities were also calculated based on the total current densities and the corresponding FE (CO) and FE (H<sub>2</sub>) (Figure 3D,E).

The intrinsic activity of the catalysts was further disclosed by the mass activities of N-C, Fe-N-C and O-Fe-N-C at –0.50 V versus RHE. Compared to N-C (0.68 A g<sup>–1</sup>) and Fe-N-C (2.2 A g<sup>–1</sup>), a much higher mass activity of 4.4 A g<sup>–1</sup> was obtained for O-Fe-N-C, revealing the axial O coordination plays a key role toward CO<sub>2</sub> RR. The smaller Tafel slope, of 29 mV dec<sup>–1</sup>, for O-Fe-N-C catalyst further indicates its favorable kinetics for the formation of CO than those of Fe-N-C (35 mV dec<sup>–1</sup>) (Figure S8, Supporting Information).<sup>[44–45]</sup>

To prove that the excellent CO<sub>2</sub> RR performance of the O-Fe-N-C catalyst was attributed to the highly dispersed single active sites rather than Fe nanoparticles or agglomerates, the O-Fe-N-C catalyst was treated with acid to remove the Fe nanoparticles. Inductively coupled plasma atomic emission spectroscopy was performed to evaluate the content of Fe in the O-Fe-N-C catalyst with and without the acid treatment (Table S2, Supporting Information). Compared to the total Fe content in the O-Fe-N-C catalyst without acid treatment (0.73 %), the content of Fe single atoms embedded in the O-Fe-N-C sample after acid treatment, decreased to 0.41 % (wt %), suggesting that the Fe nanoparticles were successfully removed. In contrast to the sharp decrease of the amount of Fe, a neglectful depression of the catalytic activity for O-Fe-N-C after the acid treatment process was observed, as shown in Figure S9 (Supporting Information), revealing the dominant impact of the exposed Fe single atoms on the high activity and selectivity. In addition, no Fe reduction/oxidation redox peaks for Fe appeared in the CV curve for the O-Fe-N-C sample (Figure S10, Supporting Information). In combination with the HAADF STEM, electron energy loss spectroscopy elemental mapping, and high-resolution TEM (HRTEM) results, it could be corroborated that the Fe clusters were rigorously encapsulated by a few layers of carbon, which would encumber the interaction between the Fe nanoparticles and the electrolyte, resulting in an inactive performance of these Fe nanoparticles (Figures S11 and S12, Supporting Information). A long-term stability test for the O-Fe-N-C electrocatalyst was performed for 30 h at a constant –0.50 V versus RHE cathode potential. The outlet gases were analyzed every 1 h by GC for calculating the corresponding FE of CO. The current density of O-Fe-N-C maintained a steady value of  $\approx -4.5$  mA cm<sup>–2</sup> with no significant decay (Figure 3F) during the 30 h test. The corresponding FE of CO decreased slightly to 88% after 30 h stability test and no liquid product was detected by <sup>1</sup>H nuclear magnetic resonance (<sup>1</sup>H-NMR) spectroscopy (Figure S13, Supporting Information).

## 2.3. Computational Studies

To further understand the intrinsic activity of the axial O group for CO<sub>2</sub> RR, DFT calculations were performed to calculate the free energies of possible intermediates in the reaction pathways from CO<sub>2</sub> to CO by using the computational hydrogen electrode model and parameters reported in the literature.<sup>[46–49]</sup> As the counterpart, we created a simulation model with an Fe atom coordinated with 4 N atoms (tetra-nitrogen) by replacing six C atoms in a graphene surface to represent the reported normal FeN<sub>4</sub> catalysts.<sup>[50]</sup> For the O-Fe-N-C catalyst, an axial –OH ligand was added to coordinate with the Fe single atom in the

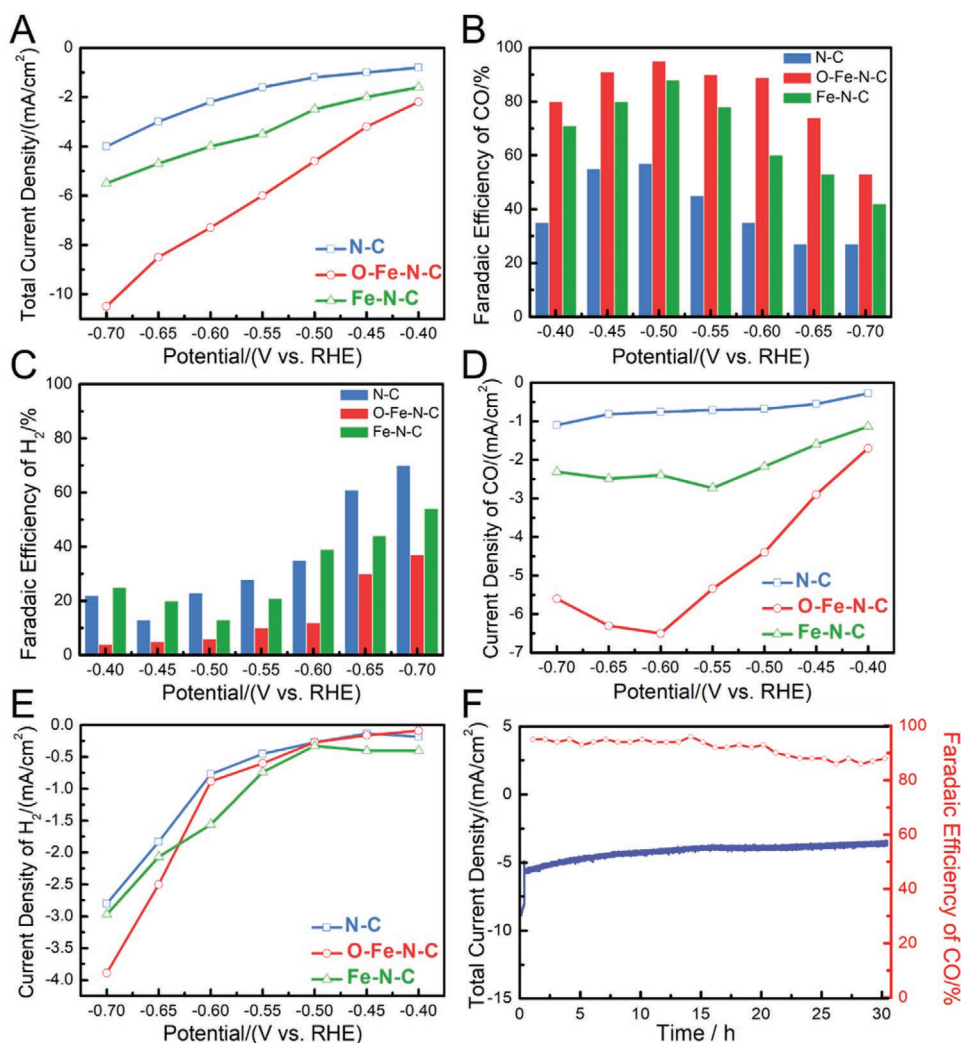


**Figure 3.** A) Total current density, B) FE of CO at various potentials, C) current density for CO production, D) FE of H<sub>2</sub> at various potentials, E) current density for H<sub>2</sub> production on N-C, O-Fe-N-C, and Fe-N-C. F) Stability test of O-Fe-N-C at -0.50 V versus RHE.

simulated FeN<sub>4</sub> catalyst model. The optimized structures and the optimal adsorption configurations of reaction intermediates are shown in Figure 4A,B. There are three elementary steps and two important intermediates (COOH\* and CO\*) involved in the CO<sub>2</sub> RR process. Their corresponding free energy profiles at a potential of 0 V versus RHE are shown in Figure 4C. The  $\Delta G$  for the formation of COOH\* over O-Fe-N-C and normal FeN<sub>4</sub> were calculated to be 0.48 and 0.15 eV, respectively. The  $\Delta G$  for the dissociation of COOH\* assisted by proton-electron transfer to produce CO\* and H<sub>2</sub>O is downhill on both catalyst models. As for the final step of CO desorption, the  $\Delta G$  over O-Fe-N-C is 0.47 eV, which is significantly lower than that over normal FeN<sub>4</sub> (0.89 eV). Under these circumstances, it is obvious that the potential determining step (PDS) is COOH\* formation ( $\Delta G = 0.48$  eV) on O-Fe-N-C, while the CO desorption step is more difficult on normal FeN<sub>4</sub> ( $\Delta G = 0.89$  eV). As the potential became more negative (-0.48 V vs RHE), the  $\Delta G$  for the formation of COOH\* decreased, whilst the  $\Delta G$  for the non-electrochemical step of CO desorption remained unchanged on both models (Figure 4D). Consequently, CO desorption became the most difficult step on both catalysts' surfaces at -0.48 V versus RHE. The

smaller  $\Delta G$  of the O-Fe-N-C catalyst (0.47 eV) than the normal FeN<sub>4</sub> (0.89 eV) indicated a superior catalytic activity for CO conversion from a thermodynamic perspective. In addition, HER as a side reaction was also considered, and its corresponding free energy profiles were shown in Figure 4E. It can be concluded that the HER is less active on O-Fe-N-C than that on normal FeN<sub>4</sub>. All these results are in good agreement with the experiments. The projected density of states (PDOS) of O-Fe-N-C and normal FeN<sub>4</sub> surfaces were calculated to investigate the origin of the difference between adsorption of the reaction intermediates over these two catalysts, and the results are shown in Figure 4F. Compared to normal FeN<sub>4</sub>, the d-band center of Fe-3d orbits shifted to a more negative value with introduction of an axial O group, which leads to weaker CO adsorption over the O-Fe-N-C, and thus improve the selectivity toward CO.<sup>[51]</sup>

### 3. Conclusions

In summary, the axial O-coordinated FeN<sub>4</sub> active site was precisely constructed by using a self-sacrificing O- and N-rich

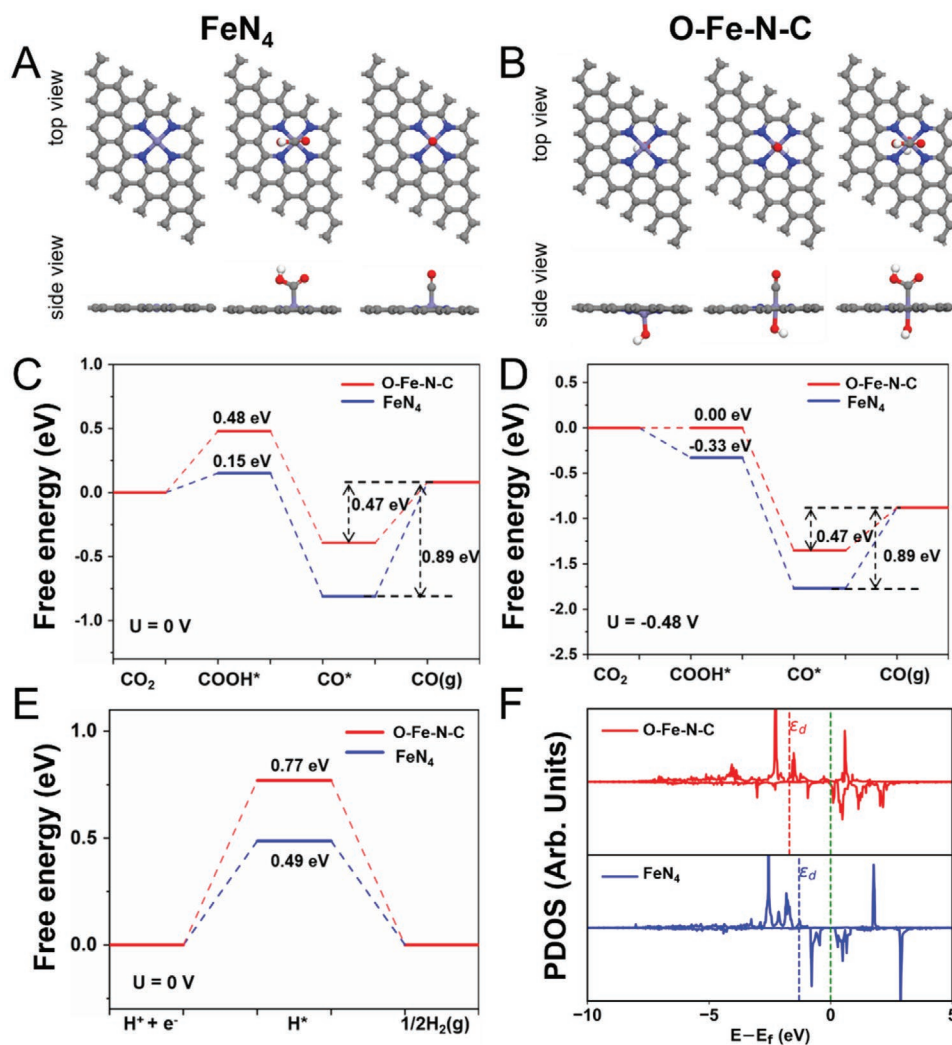


**Figure 4.** A,B) Top view and side view optimized adsorption configuration on simulated FeN<sub>4</sub> and O-Fe-N-C (Fe, O, N, and C atoms are represented in purple, red, blue, and gray, respectively). C) Free energy profiles for the CO<sub>2</sub> RR to CO at 0 V (vs RHE) and D) Free energy profiles for the CO<sub>2</sub> RR to CO at -0.48 V (vs RHE). E) Free energy profiles for the HER at 0 V (vs RHE) on simulated FeN<sub>4</sub> and O-Fe-N-C. F) Projected d-density of states (PDOS) of Fe over O-Fe-N-C and FeN<sub>4</sub> surfaces.

IRMOF-3. The obtained FeN<sub>4</sub>-O sites were experimentally proved to be much more active than the FeN<sub>4</sub> active sites, showing an excellent FE (CO) of 95% at a low applied potential of -0.50 V versus RHE. Such performance outperforms previously reported Fe-N-C-based catalysts and most of the reported single atom catalysts at lower overpotential. Meanwhile, DFT simulations revealed that the axial O coordination could not only weaken the binding energy of CO but also inhibit the competitive hydrogen evolution. This work opens a new way for engineering the coordination of FeN<sub>4</sub> sites via heteroatom-rich MOFs precursors.

## Supporting Information

Supporting Information is available from the Wiley Online Library or from the author.

## Acknowledgements

T.Z., X.H., and H.L. contributed equally to this work. ICN2 acknowledges funding from Generalitat de Catalunya 2017 SGR 327. IREC acknowledges Generalitat de Catalunya for financial support M2E 2017 SGR 1246. T.Z., J.R.M., and J.A. thank support from the project NANOGEN (PID2020-116093RB-C43), funded by MCIN/AEI/10.13039/501100011033/. ICN2 was supported by the Severo Ochoa program from Spanish MINECO (Grant No. SEV-2017-0706). ICN2 and IREC were funded by the CERCA Programme/Generalitat de Catalunya. This project received funding from the European Union's Horizon research and innovation programme under Grant Agreement No. 823717-ESTEEM3. J.L. acknowledges funding from the European Union's Horizon 2020 research and innovation programme under the Marie Skłodowska-Curie Grant Agreement No 101030637. X.Z. acknowledges funding from FWO project (12ZV320N). Part of the present work was performed in the framework of Universitat Autònoma de Barcelona Materials Science Ph.D. program. T.Z. and X.H. thank China Scholarship Council for scholarship support (201706180028, 201804910551). The authors thank Guillaume Sauthier, Javier Saiz, and Yunhui Yang for the XPS spectrum, FTIR, and <sup>1</sup>H-NMR tests.

## Conflict of Interest

The authors declare no conflict of interest.

## Data Availability Statement

The data that support the findings of this study are available from the corresponding author upon reasonable request.

## Keywords

CO generation, CO<sub>2</sub> electroreduction, FeN<sub>4</sub>-O active sites, metal–organic frameworks, single atom catalysts

Received: November 10, 2021

Revised: December 16, 2021

Published online: January 22, 2022

- [1] Q. Guo, F. Liang, X.-B. Li, Y.-J. Gao, M.-Y. Huang, Y. Wang, S.-G. Xia, X.-Y. Gao, Q.-C. Gan, Z.-S. Lin, C.-H. Tung, L.-Z. Wu, *Chem* **2019**, *5*, 2605.
- [2] H. B. Yang, S.-F. Hung, S. Liu, K. Yuan, S. Miao, L. Zhang, X. Huang, H.-Y. Wang, W. Cai, R. Chen, J. Gao, X. Yang, W. Chen, Y. Huang, H. M. Chen, C. M. Li, T. Zhang, B. Liu, *Nat. Energy* **2018**, *3*, 140.
- [3] D. U. Nielsen, X.-M. Hu, K. Daasbjerg, T. Skrydstrup, *Nat. Catal.* **2018**, *1*, 244.
- [4] B. You, Y. Sun, *Acc. Chem. Res.* **2018**, *51*, 1571.
- [5] Q. Cheng, K. Mao, L. Ma, L. Yang, L. Zou, Z. Zou, Z. Hu, H. Yang, *ACS Energy Lett.* **2018**, *3*, 1205.
- [6] J. Huang, R. Buonsanti, *Chem. Mater.* **2019**, *31*, 13.
- [7] J. Pei, T. Wang, R. Sui, X. Zhang, D. Zhou, F. Qin, X. Zhao, Q. Liu, W. Yan, J. Dong, L. Zheng, A. Li, J. Mao, W. Zhu, W. Chen, Z. Zhuang, *Energy Environ. Sci.* **2021**, *14*, 3019.
- [8] C. Zhao, X. Dai, T. Yao, W. Chen, X. Wang, J. Wang, J. Yang, S. Wei, Y. Wu, Y. Li, *J. Am. Chem. Soc.* **2017**, *139*, 8078.
- [9] T. Zhang, X. Han, H. Liu, M. Biset-Peiró, X. Zhang, P. Tan, P. Tang, B. Yang, L. Zheng, J. R. Morante, J. Arbiol, *Energy Environ. Sci.* **2021**, *14*, 4847.
- [10] A. S. Varela, W. Ju, A. Bagger, P. Franco, J. Rossmeisl, P. Strasser, *ACS Catal.* **2019**, *9*, 7270.
- [11] M. Li, H. Wang, W. Luo, P. C. Sherrell, J. Chen, J. Yang, *Adv. Mater.* **2020**, *32*, 2001848.
- [12] G. Zhang, Y. Jia, C. Zhang, X. Xiong, K. Sun, R. Chen, W. Chen, Y. Kuang, L. Zheng, H. Tang, W. Liu, J. Liu, X. Sun, W.-F. Lin, H. Dai, *Energy Environ. Sci.* **2019**, *12*, 1317.
- [13] T. N. Nguyen, M. Salehi, Q. V. Le, A. Seifitokaldani, C. T. Dinh, *ACS Catal.* **2020**, *10*, 10068.
- [14] X.-M. Hu, H. H. Hval, E. T. Bjerglund, K. J. Dalgaard, M. R. Madsen, M.-M. Pohl, E. Welter, P. Lamagni, K. B. Buhl, M. Bremholm, M. Beller, S. U. Pedersen, T. Skrydstrup, K. Daasbjerg, *ACS Catal.* **2018**, *8*, 6255.
- [15] F. Pan, H. Zhang, K. Liu, D. Cullen, K. More, M. Wang, Z. Feng, G. Wang, G. Wu, Y. Li, *ACS Catal.* **2018**, *8*, 3116.
- [16] X. Yang, J. Cheng, X. Xuan, N. Liu, J. Liu, *ACS Sustainable Chem. Eng.* **2020**, *8*, 10536.
- [17] Y. Wu, C. Chen, X. Yan, X. Sun, Q. Zhu, P. Li, Y. Li, S. Liu, J. Ma, Y. Huang, B. Han, *Angew. Chem., Int. Ed.* **2021**, *60*, 20803.
- [18] H. Zhang, J. Li, S. Xi, Y. Du, X. Hai, J. Wang, H. Xu, G. Wu, J. Zhang, J. Lu, J. Wang, *Angew. Chem., Int. Ed.* **2019**, *58*, 14871.
- [19] Y. Pan, R. Lin, Y. Chen, S. Liu, W. Zhu, X. Cao, W. Chen, K. Wu, W.-C. Cheong, Y. Wang, L. Zheng, J. Luo, Y. Lin, Y. Liu, C. Liu, J. Li, Q. Lu, X. Chen, D. Wang, Q. Peng, C. Chen, Y. Li, *J. Am. Chem. Soc.* **2018**, *140*, 4218.
- [20] H. Chen, X. Guo, X. Kong, Y. Xing, Y. Liu, B. Yu, Q.-X. Li, Z. Geng, R. Si, J. Zeng, *Green Chem.* **2020**, *22*, 7529.
- [21] Qu, S. J. i, Y. Chen, D. Wang, Y. Li, *Chem. Sci.* **2021**, *12*, 4201.
- [22] Z. Chen, A. Huang, K. Yu, T. Cui, Z. Zhuang, S. Liu, J. Li, R. Tu, K. Sun, X. Tan, J. Zhang, D. Liu, Y. Zhang, P. Jiang, Y. Pan, C. Chen, Q. Peng, Y. Li, *Energy Environ. Sci.* **2021**, *14*, 3430.
- [23] X. Wang, Y. Pan, H. Ning, H. Wang, D. Guo, W. Wang, Z. Yang, Q. Zhao, B. Zhang, L. Zheng, J. Zhang, *Appl. Catal., B* **2020**, *266*, 118630.
- [24] S. Ji, Y. Chen, X. Wang, Z. Zhang, D. Wang, Y. Li, *Chem. Rev.* **2020**, *120*, 11900.
- [25] Y.-S. Wei, M. Zhang, R. Zou, Q. Xu, *Chem. Rev.* **2020**, *120*, 12089.
- [26] C.-C. Hou, H.-F. Wang, C. Li, Q. Xu, *Energy Environ. Sci.* **2020**, *13*, 1658.
- [27] L. Jiao, H.-L. Jiang, *Chem* **2019**, *5*, 786.
- [28] L. Zou, Y.-S. Wei, C.-C. Hou, C. Li, Q. Xu, *Small* **2021**, *17*, 2004809.
- [29] L. Ye, Y. Ying, D. Sun, Z. Zhang, L. Fei, Z. Wen, J. Qiao, H. Huang, *Angew. Chem., Int. Ed.* **2020**, *59*, 3244.
- [30] W. Ren, X. Tan, W. Yang, C. Jia, S. Xu, K. Wang, S. C. Smith, C. Zhao, *Angew. Chem., Int. Ed.* **2019**, *58*, 6972.
- [31] X. Ao, W. Zhang, Z. Li, J.-G. Li, L. Soule, X. Huang, W.-H. Chiang, H. M. Chen, C. Wang, M. Liu, X. C. Zeng, *ACS Nano* **2019**, *13*, 11853.
- [32] C. Zhao, Y. Wang, Z. Li, W. Chen, Q. Xu, D. He, D. Xi, Q. Zhang, T. Yuan, Y. Qu, J. Yang, F. Zhou, Z. Yang, X. Wang, J. Wang, J. Luo, Y. Li, H. Duan, Y. Wu, Y. Li, *Joule* **2019**, *3*, 584.
- [33] L. Gong, H. Zhang, Y. Wang, E. Luo, K. Li, L. Gao, Y. Wang, Z. Wu, Z. Jin, J. Ge, Z. Jiang, C. Liu, W. Xing, *Angew. Chem., Int. Ed.* **2020**, *59*, 13923.
- [34] Y. Lou, J. Liu, M. Liu, F. Wang, *ACS Catal.* **2020**, *10*, 2443.
- [35] J. Wang, R. You, C. Zhao, W. Zhang, W. Liu, X.-P. Fu, Y. Li, F. Zhou, X. Zheng, Q. Xu, T. Yao, C.-J. Jia, Y.-G. Wang, W. Huang, Y. Wu, *ACS Catal.* **2020**, *10*, 2754.
- [36] Q. Wang, T. Ina, W.-T. Chen, L. Shang, F. Sun, S. Wei, D. Sun-Waterhouse, S. G. Telfer, T. Zhang, G. I. N. Waterhouse, *Sci. Bull.* **2020**, *65*, 1743.
- [37] P. Yin, T. Yao, Y. Wu, L. Zheng, Y. Lin, W. Liu, H. Ju, J. Zhu, X. Hong, Z. Deng, G. Zhou, S. Wei, Y. Li, *Angew. Chem., Int. Ed.* **2016**, *55*, 10800.
- [38] X. X. Wang, D. A. Cullen, Y.-T. Pan, S. Hwang, M. Wang, Z. Feng, J. Wang, M. H. Engelhard, H. Zhang, Y. He, Y. Shao, D. Su, K. L. More, J. S. Spendelow, G. Wu, *Adv. Mater.* **2018**, *30*, 1706758.
- [39] J. Li, M. Chen, D. A. Cullen, S. Hwang, M. Wang, B. Li, K. Liu, S. Karakalos, M. Lucero, H. Zhang, C. Lei, H. Xu, G. E. Sterbinsky, Z. Feng, D. Su, K. L. More, G. Wang, Z. Wang, G. Wu, *Nat. Catal.* **2018**, *1*, 935.
- [40] L. Jiao, G. Wan, R. Zhang, H. Zhou, S.-H. Yu, H.-L. Jiang, *Angew. Chem., Int. Ed.* **2018**, *57*, 8525.
- [41] J. Li, P. Pršljaja, T. Shinagawa, A. J. M. Fernández, F. Krumeich, K. Artyushkova, P. Atanassov, A. Zitolo, Y. Zhou, R. García-Muelas, N. López, J. Pérez-Ramírez, F. Jaouen, *ACS Catal.* **2019**, *9*, 10426.
- [42] Y. Chen, S. Ji, Y. Wang, J. Dong, W. Chen, Z. Li, R. Shen, L. Zheng, Z. Zhuang, D. Wang, Y. Li, *Angew. Chem., Int. Ed.* **2017**, *56*, 6937.
- [43] O. S. Bushuyev, P. De Luna, C. T. Dinh, L. Tao, G. Saur, J. van de Lagemaat, S. O. Kelley, E. H. Sargent, *Joule* **2018**, *2*, 825.



- [44] J. Gu, C.-S. Hsu, L. Bai, H. M. Chen, X. Hu, *Science* **2019**, *364*, 1091.
- [45] C. W. Li, M. W. Kanan, *J. Am. Chem. Soc.* **2012**, *134*, 7231.
- [46] J. K. Nørskov, J. Rossmeisl, A. Logadottir, L. Lindqvist, J. R. Kitchin, T. Bligaard, H. Jónsson, *J. Phys. Chem. B* **2004**, *108*, 17886.
- [47] H. Liu, J. Liu, B. Yang, *Phys. Chem. Chem. Phys.* **2019**, *21*, 9876.
- [48] H. Liu, J. Liu, B. Yang, *Phys. Chem. Chem. Phys.* **2020**, *22*, 9600.
- [49] J. Li, A. Slassi, X. Han, D. Cornil, M.-H. Ha-Thi, T. Pino, D. P. Debecker, C. Colbeau-Justin, J. Arbiol, J. Cornil, M. N. Ghazzal, *Adv. Funct. Mater.* **2021**, *31*, 2100994.
- [50] J. Li, J. Liu, B. Yang, *J. Energy Chem.* **2021**, *53*, 20.
- [51] X. Liu, H. Liu, C. Chen, L. Zou, Y. Li, Q. Zhang, B. Yang, Z. Zou, H. Yang, *Nano Res.* **2019**, *12*, 1651.